# Rich active-edge-site MoS$_2$ anchored on reduction sites in metal sulfide heterostructure: Toward robust visible light photocatalytic hydrogen sulphide splitting

Meng Dan[a,b], Jianglai Xiang[a,b], Fan Wu[b], Shan Yu[b], Qing Cai[b], Liqun Ye[c], Yinghao Ye[b], Ying Zhou[a,b,*]

[a] State Key Laboratory of Oil and Gas Reservoir Geology and Exploitation, Southwest Petroleum University, Chengdu 610500, China
[b] The Center of New Energy Materials and Technology, School of Materials Science and Engineering, Southwest Petroleum University, Chengdu 610500, China
[c] Engineering Technology Research Center of Henan Province for Solar Catalysis, College of Chemistry and Pharmaceutical Engineering, Nanyang Normal University, Nanyang 473061, China

## ARTICLE INFO

## ABSTRACT

In this work, the unsaturated-sulfur-edge-rich (U$_S$-rich) MoS$_2$ was successfully introduced in MnS/In$_2$S$_3$ composites by a smart S-vacancies-induced strategy. The surface chemical state analysis, photoluminescence (PL) spectra and electron spin resonance (ESR) spectra confirm that the MoS$_2$ with rich U$_S$ can selectively grow on the MnS of MnS/In$_2$S$_3$ composites resulting in the formation of a typical double-interface-structure. The linear sweep voltammetry (LSV) test confirms that the U$_S$-rich MoS$_2$ processed superior proton reduction activity. Moreover, the superb charge transfer efficiency from MnS to MoS$_2$ and remarkable HS$^-$ adsorption performance were verified by the density functional theory (DFT) calculations. As a result, the novel MnS/In$_2$S$_3$-MoS$_2$ (denoted as MI-M) is the state-of-the-art non-noble-metal visible light driven photocatalysts with H$_2$ evolution rate of 124 μmol h$^{-1}$ from H$_2$S which is 4.5 times higher than that of the pristine MnS/In$_2$S$_3$ heterostructure. The corresponding apparent quantum efficiency (AQE) at 400 nm is as high as 72%.

## 1. Introduction

The industrialization of human society has generated concerns regarding aggravated energy crisis and worsening environmental problems caused by the consumption of fossil-fuel and rapid depletion of non-renewable resources. The elimination of pollutants has become a key point to global concern and many efforts have thus been dedicated to decompose the pollutants and remediate the environment. However, many of the pollutants are potentially valuable chemicals with rich energy. For instance, Hydrogen sulphide (H$_2$S) is a detrimental and undesirable chemical, while it can be converted into clean energy (H$_2$) and elemental sulfur, exerting economic and environmental value [1–4]. In recent years, photocatalytic hydrogen production (PHP) from waste H$_2$S has been considered to be an appealing and sustainable approach to develop clean hydrogen energy (H$_2$) to replace fossil fuels and remove toxic pollutant H$_2$S gas [5–8]. Despite numerous impressed photocatalysts have been explored, their PHP efficiency is still thwarted to a large extent by the undesirable electron-hole recombination due to the random charge flow and limited reaction active sites [9–11].

Therefore, it remains a high challenge to manipulate the charge flow simultaneously with the optimization of catalytically active sites.

As one of the solutions to address these issues, loading cocatalysts on the photocatalyst surface to form a Schottky junction is confirmed to be an efficient strategy [12–14]. Among them, the noble-metals such as Ru, Au, and Pt, etc [15–17]. are widely used as cocatalysts because of their low Gibbs' free energy of absorbed H atoms [18–20]. However, the scarcity and high-cost of noble-metals considerably impede their large-scale utilization for PHP. More importantly, these noble metal cocatalysts are usually unstable during H$_2$S splitting process due to the poisoning effect of H$_2$S [8,11]. Therefore, the development of noble-metal-free cocatalysts with desirable efficiency and excellent stability is generally required. Molybdenum sulfide (MoS$_2$), emerging as an earth abundant and environmental friendly alternative to noble metal, exhibits compelling potential as a cocatalyst for PHP reaction considering its free energy similar to that of Pt, which is close to zero [21,22]. Moreover, the exposed edges of MoS$_2$ can act as reaction active sites for boosting photocatalytic reaction because of its edge structure closely resembling that of hydrogen-producing enzymes found in nature

---

[23–25]. Moreover, $MoS_2$ is very stable in the $H_2S$-containing medium exempting the poisoning effect of $H_2S$ [5,8,11]. Consequently, tremendous endeavor has been devoted to craft highly efficient $MoS_2$/semiconductor photocatalyst. Among them, the defect-induced growth strategy is deemed to be one of the highly promising methods to construct $MoS_2$/semiconductor composites with intimate contact [26–31]. For instance, Park and Lee used the surface and subsurface defects in CdS to induce epitaxial growth of $MoS_2$ for promoting solar hydrogen production [32]. Liu et al. reported that $MoS_2$ quantum dot growth induced by S vacancies in a $ZnIn_2S_4$ monolayer exhibited excellent photocatalytic performance [33]. These reports indicate that the introduction of $MoS_2$ cocatalyst enables to enhance the photocatalytic performance to some extent. However, the photocatalytic performance of $MoS_2$ is dependent on the density of active-edge-site [34,35]. Furthermore, the charge separation efficiency is unsatisfactory because of the close contact between the electron acceptor ($MoS_2$) and hole acceptor (substrate catalysts). Therefore, the effect of $MoS_2$ cocatalysts for electron transfer is partially limited in these works [26–33]. In our previous work [36], an novel two-dimensional (2D) $MnS/In_2S_3$ layer heterostructure was successfully established with remarkable visible-light photocatalytic $H_2S$ splitting performance. Moreover, the photo-oxidation and photo-reduction reaction have been demonstrated to take place on MnS and $In_2S_3$, respectively. Taking into account these, if the $MoS_2$ with abundant reaction active sites were selectively decorated on MnS (reduction sites) in $MnS/In_2S_3$ composite, the photogenerated electrons can further migrate to $MoS_2$ nanosheet. Thus, it is expected that the novel $MnS/In_2S_3$-$MoS_2$ composites with rich catalytically active sites can be obtained by the defect-induced growth strategy for accelerating PHP performance from $H_2S$ splitting.

Herein, a defect-induced growth strategy was used to deposit the unsaturated-sulfur-edge-rich $MoS_2$ ($U_S$-rich $MoS_2$) nanosheet at the S vacancies on MnS in $MnS/In_2S_3$ composite to craft novel $MnS/In_2S_3$-$MoS_2$ (denoted as MI-M) composite for the first time. The electrons and holes from visible-light irradiated $MnS/In_2S_3$ composites are spatially separated by the internal electric field built between MnS and $In_2S_3$, with the electrons further transferring to $MoS_2$ cocatalyst. Hence, the electric flow regulating can be well implemented by the construction of double-interface-structure. Moreover, the abundant reaction active sites are provided due to the existence of rich unsaturated active S atoms. As a result, the MI-M composite showed a superior photocatalytic $H_2$ evolution activity ($124 \, \mu mol \, h^{-1}$) from decomposition of waste $H_2S$, which is almost 4.5 times higher than that of the pristine $MnS/In_2S_3$. The corresponding apparent quantum efficiency (AQE) at 400 nm is 72%, which is the highest visible-light-driven photocatalytic $H_2S$ splitting efficiency reported so far among all kinds of non-noble-metal photocatalysts. Meanwhile, the electrochemical measurements are also performed to confirm the $U_S$-rich $MoS_2$ can act as proper cocatalyst to promote the $H_2$ production. This work is anticipated to give deep insights into understanding the charge transfer in cocatalyst/semiconductor composites and rationally designing advanced photocatalysts for superior photocatalytic $H_2S$ splitting.

## 2. Experimental section

### 2.1. Synthesis of MnS/In₂S₃ nanosheets

The pristine $MnS/In_2S_3$ nanosheets were prepared by a facile solvothermal method [36]. $Mn(Ac)_2 \cdot 4H_2O$ (1.4 mmol), $InCl_3$ (0.6 mmol) and thioacetamide (TAA) (9.0 mmol) were dissolved in 25 mL pyridine to form a homogeneous solution. Subsequently, the obtained solution was immediately transferred to a 50 mL Teflon-lined stainless steel autoclave and maintained at 180 °C for 30 h. After cooling to room temperature, the prepared precipitates were centrifuged and washed several times with ethanol. Finally, the collected solid was dried at 50 °C for 10 h to obtain $MnS/In_2S_3$.

### 2.2. Synthesis of MnS/In₂S₃-MoS₂ composites

In a typical procedure, 200 mg synthesized $MnS/In_2S_3$ powders were dissolved in 25 mL pyridine. After stirring for 30 min, the different contents of $MoS_2$ precursors (TAA and $Na_2MoO_4$) were immersed in the above solution. The solution was transferred into a Teflon-lined autoclave and maintained at 180 °C for 30 h. After cooling to room temperature, the prepared precipitates were centrifuged and washed several times with ethanol, and dried in a vacuum oven at 50 °C for 10 h to obtained $MnS/In_2S_3$-$MoS_2$ composites with different amount of $MoS_2$ nanosheets. For convenience, the $MnS/In_2S_3$-$MoS_2$ composites were denoted as MI-Mx, where x represent the weight percentages of $MoS_2$ in the composites (MI-Mx, x = 1.5: 3.9 mg of $Na_2MoO_4$ and 9 mg of TAA; x = 3.0: 7.8 mg of $Na_2MoO_4$ and 9 mg of TAA; x = 4.5: 11.7 mg of $Na_2MoO_4$ and 9 mg of TAA; x = 6.0: 15.6 mg of $Na_2MoO_4$ and 9 mg of TAA). For comparison, $MnS$-$MoS_2$ and $In_2S_3$-$MoS_2$ samples were also prepared under similar conditions.

### 2.3. Characterization

The power X-ray diffraction (XRD) (PANalyticalX'pert) with Cu Kα radiation operated at 40 kV/40 mA was performed to investigate the crystal structure and crystallinity of the samples. The X-ray photoelectron spectroscopy (XPS) measurements were performed to investigate the surface chemical composition and all of the binding energies were referenced to the C 1s level at 284.8 eV. Transmission electron microscopy (TEM) observation was conducted on a Tecnai G2 F30 electron microscopy with an accelerating voltage of 200 kV. Energy dispersive X-ray spectroscopy (EDS) was used to obtain elemental mapping. UV–vis diffuse reflectance spectra (DRS) were recorded on a Shimadzu UV-2600 spectrophotometer equipped with an integrating sphere using $Ba_2SO_4$ as the reflectance standard. The electron spin resonance (ESR) spectra were recorded on a JES-FA200 Electron Spin Resonance Spectrometer operating at about 9.0 GHz at room temperature. The photoluminescence (PL) spectra were tested with a fluorescence spectrophotometer (Nicolet 6700, excitation at 400 nm). The surface photovoltage (SPV) spectra were obtained by a TLS-SPV530 spectrometer (Zolix Instruments Co., Beijing). The $N_2$ adsorption-desorption isotherm and pore-size distributions were measured via the nitrogen adsorption method (Quadrasorb S1). The samples were degassed at 110 °C for 24 h under vacuum before measurements.

### 2.4. DFT calculation

The density functional theory (DFT) calculations were performed using the generalized gradient approximation (GGA) exchange-correlation functional of the Perdew-Burke-Ernzerhof (PBE) type as implemented in the Cambridge Sequential Total Energy Package (CASTEP) [37,38]. The Brillouin zone was elected with $2 \times 2 \times 1$ Monkhorst-Pack $k$-point grids for the structure optimizations. The cutoff energy of the plane-wave expansion was set to 400 eV. All geometries were adequately optimized until the convergence criteria of energy and force reached $1 \times 10^{-5}$ eV and 0.02 eV/Å, respectively. The neighboring system interference along the c axis was avoided by building a vacuum space of 20 Å. The first-principles DFT simulation was carried out based on constructed crystal structures of the MnS (001) and $MoS_2$ (001) surfaces.

### 2.5. Photocatalytic performance evaluations

The photocatalytic activity measurements were conducted in a home-made photoreactor (50 mL Pyrex flask), as shown in Fig. S7. Firstly, 2.5 mg of catalyst powders were suspended through ultrasonication for 25 min in an aqueous solution (50 mL, 0.1 mol·$L^{-1}$ $Na_2S$/0.6 mol·$L^{-1}$$Na_2SO_3$). Then, the reactor was purged with Ar for 30 min followed by bubbling 3 M $H_2S$ in the solution for 3 h at room

temperature. Finally, the reactor was illuminated by a 300-W Xe lamp with a cutoff filter ($\lambda > 420$ nm). The amount of produced hydrogen was monitored using a Shimadzu GC-2010Plus gas chromatograph (Ar carrier gas, molecular sieve 5 Å, TCD detector).

### 2.6. The apparent quantum efficiency (AQE)

The AQE was calculated according to Eq. (1). The number of evolved $H_2$ molecules was measured by GC (Shimadzu GC-2010 Plus) and the number of incident photons was determined from the output of a monochromatic LED lamp.

$$
\begin{aligned}
\text{AQE}(\%) &= \frac{\text{number of reacted electrons}}{\text{number of incident photos}} \\
&= \frac{2 \times \text{number of evolved} H_2 \text{molecules}}{\text{number of incident photons}} \times 100
\end{aligned}
\tag{1}
$$

### 2.7. Photoeletrochemical measurements

The Electro-chemical impedance spectroscopy (EIS) and Transient photocurrent response were investigated with CHI660E workstation by using Pt wire as a counter, and saturated calomel electrode as reference electrode. The working electrode with an active area of ca. 1 cm$^2$ was prepared by a doctor blading technique (FTO, film thickness: 50 μm). The 1.2 M $Na_2SO_3$ was used as electrolyte. The Electro-chemical impedance spectroscopy (EIS) and Transient photocurrent responseover all the samples at open circuit potential were tested under visible-light irradiation ($\lambda > 420$ nm). Linear sweep voltammetry (LSV) was carried out at a scan rate of 10 mV/s. Chronopotentiometric measurement is conducted by maintaining the current density at 10 mA cm$^{-2}$.

## 3. Results and discussion

A series of MnS/$In_2S_3$-$MoS_2$ composites denoted as MI-Mx (x = 1.5, 3.0, 4.5, 6.0), where x stands for loading amount of $MoS_2$ in the MnS/$In_2S_3$ composite (See Experimental Section for more detailed information), were investigated by XRD to unravel the possible Mo species existing in the MnS/$In_2S_3$ composite. As shown in Fig. S1, all MI-Mx samples exhibit a similar structure with the pristine MnS/$In_2S_3$. All diffraction patterns can be indexed to the hexagonal γ-MnS (JCPDS 40-1289) and β-$In_2S_3$ (JCPDS 65-0459), which agree well with the previous work [36]. Interestingly, no diffraction peaks assigned to $MoS_2$ or any other Mo-relating phases were observed, illustrating that Mo in MI-M composites are either highly dispersed or low crystalline. Additionally, the formation of $MoS_2$ can be certificated by the diffraction features attributable to $MoS_2$ (JCPDS 37-1492) in the absence of MnS/$In_2S_3$ (Fig. S2), suggesting that $MoS_2$ can be successfully obtained under this synthesis condition. Nevertheless, it is noteworthy that the substantial shift of diffraction peaks of $MoS_2$ ((002) plane) is observed as compared to commercial $MoS_2$. The results illustrate that the as-prepared $MoS_2$ could consist of single or few layers, which favors to provide abundant catalytically active sites.

It has been confirmed in previous studies that $MoS_2$ can be selectively deposited on the sulfur vacancy (Vs) because of the inductive effect between $MoO_4^{2-}$ and $V_S$ [32,33]. In the present work, the $Na_2MoO_4$ is elected as the Mo source of $MoS_2$. The situation of $MoS_2$ was explored by disclosing the existence of $V_S$ in MnS/$In_2S_3$ composite through the combination of UV–vis DRS, PL, and ESR characterizations. Different from $In_2S_3$, two obvious absorption peaks in the visible light range (between 450 and 700 nm) are observed for MnS, which could be attributed to the defects in MnS crystals (Fig. S3) [36]. This illustrates that the MnS possesses rich defects as compared to $In_2S_3$. The room-temperature ESR was performed to further investigate the type and existence of defects. As reflected by Fig. 1a, the MnS shows a strong ESR signal, giving the g-value of as 2.003 (Fig. 1a), which is ascribed to the

surface S-vacancies [33,39]. Moreover, rich S vacancies are proven to be still present in 2D MnS/$In_2S_3$ composite in comparison the ESR signal of MnS/$In_2S_3$ with that of pristine MnS. However, such ESR signal cannot be found in the $In_2S_3$. The above results demonstrate that the $V_S$ are primarily originated from the MnS in the MnS/$In_2S_3$ composite. Correspondingly, it can be affirmed that the $MoS_2$ should be prone to selectively grow on MnS in MnS/$In_2S_3$ composite. Notably, the ESR intensity of MI-M4.5 is much stronger than that of the pristine MnS/$In_2S_3$, implying that the introduction of $MoS_2$ brings more $V_S$ into MI-M4.5 as a result of the formation of $U_S$-rich $MoS_2$. The PL measurement is also carried out to identify the existence and relative amount of $V_S$. As shown in Fig. 1b, the $MoS_2$ exhibits strong PL emission at around 600 nm, which could be attributed to the $V_S$ induced by the $U_S$ [3,10,36,40,41]. After deposition of $MoS_2$ on MnS/$In_2S_3$, the PL intensity increased with augmenting the amount of $MoS_2$. This result further indicates that the MI-M composites with $U_S$-rich $MoS_2$ involved are achievable through this synthetic method. On the basis of above analysis, the formation mechanism of the MI-M composite is depicted in Fig. 1c. First, thioacetamide (TAA) and $Na_2MoO_4$ are used as the precursors of $MoS_2$ which are immersed in the homogeneous dispersion of MnS/$In_2S_3$. Subsequently, the $MoO_4^{2-}$ is selectively deposited on the Vs region of MnS in MnS/$In_2S_3$ composite. Finally, the novel MI-M double-interface-structure with rich catalytically active sites is obtained by a typical heat treatment process.

In order to gain a better understanding of the existing $MoS_2$ in MI-M composite, XPS measurements were conducted. Fig. 2a shows the XPS survey spectrum of $MoS_2$, MnS/$In_2S_3$ and MI-M4.5. The existence of Mo element is not significantly observed in the MI-M4.5 composite due to the low loading amount of $MoS_2$ and the shielding by strong S 1 s signal, but it can be revealed by the high-resolution XPS spectra of Mo 3d (Fig. 2f). The Mo 3d spectra can be deconvoluted into three pairs of peaks which are assigned to signals for $Mo^{6+}$ (235.6 and 232.4 eV), $Mo^{5+}$ (233.1 and 229.6 eV), and $Mo^{4+}$ (232.7 and 229.5 eV) in $MoS_2$, respectively [42]. The high valence state of Mo ($Mo^{6+}$ and $Mo^{5+}$) can be attributed to the low-coordination S resulting from escape of S atoms [33,43,44]. It has to be pointed out here that only the feature of $Mo^{6+}$ (235.1 (Mo $3d_{3/2}$), 232.5 eV (Mo $3d_{5/2}$)) existed after growing $MoS_2$ onto MnS/$In_2S_3$ composite, presumably owing to the increasing amount of exposed edges of $MoS_2$ in MI-M composites. This result is further confirmed by the S 2p core spectra of $MoS_2$, MnS/$In_2S_3$, and MI-M4.5 (Fig. 2c). The higher binding energy (163.2 eV) is ascribed to the unsaturated $S_2^{2-}$ from the $MoS_2$ and the lower binding energy signal to shared $S^{2-}$ in the sulphides [45]. These results indicate that $MoS_2$ with rich $U_S$ are formed in MI-M composites, affording more reactive active sites for catalytic reaction [25]. The observation of fine XPS spectra for Mn 2p (Fig. 2d) and In 3d (Fig. 2e) in MnS/$In_2S_3$ and MI-M4.5 clarifies that the binding energy of Mn 2p in MI-M4.5 is beyond 0.6 eV higher than that of the pristine MnS/$In_2S_3$, while those of In 3d remains unchanged (Fig. 2e). The results again implied that the $MoS_2$ can be selectively grown on MnS in MnS/$In_2S_3$ composite. From the XPS valence band (VB) spectra of MnS/$in_2S_3$ composite related with the features of $In_2S_3$ [36], it can be found that the VB position does not change despite the introduction of $MoS_2$ (Fig. 2b), further indicative of the selective decoration of $U_S$-rich $MoS_2$ on MnS instead of $In_2S_3$.

To close observation the morphology and interface structure of MI-M samples, TEM and high resolution TEM (HRTEM) images were recorded as shown in Fig. 3 and Fig. S4-5. Both $MoS_2$ and MnS/$In_2S_3$ exhibit the nanosheet morphology (Fig. S4a and Fig. S5a), which is favourable to construct the 2D-2D interface system between $MoS_2$ and MnS/$In_2S_3$ with intimate contact. Moreover, the $MoS_2$ shows folded layers with extensive wrinkles due to the existence of abundant $U_S$ defect. Fringes with lattice spacing of 6.8 Å displayed in Fig. S4b corresponds to the (002) plane of hexagonal $MoS_2$. The nanosheet structure of MnS/$In_2S_3$ is preserved after the decoration of $MoS_2$ as reflected by TEM images in Fig. 3a, illustrating that the morphology of MnS/$In_2S_3$ is not influenced by introducing of $MoS_2$, which is also confirmed
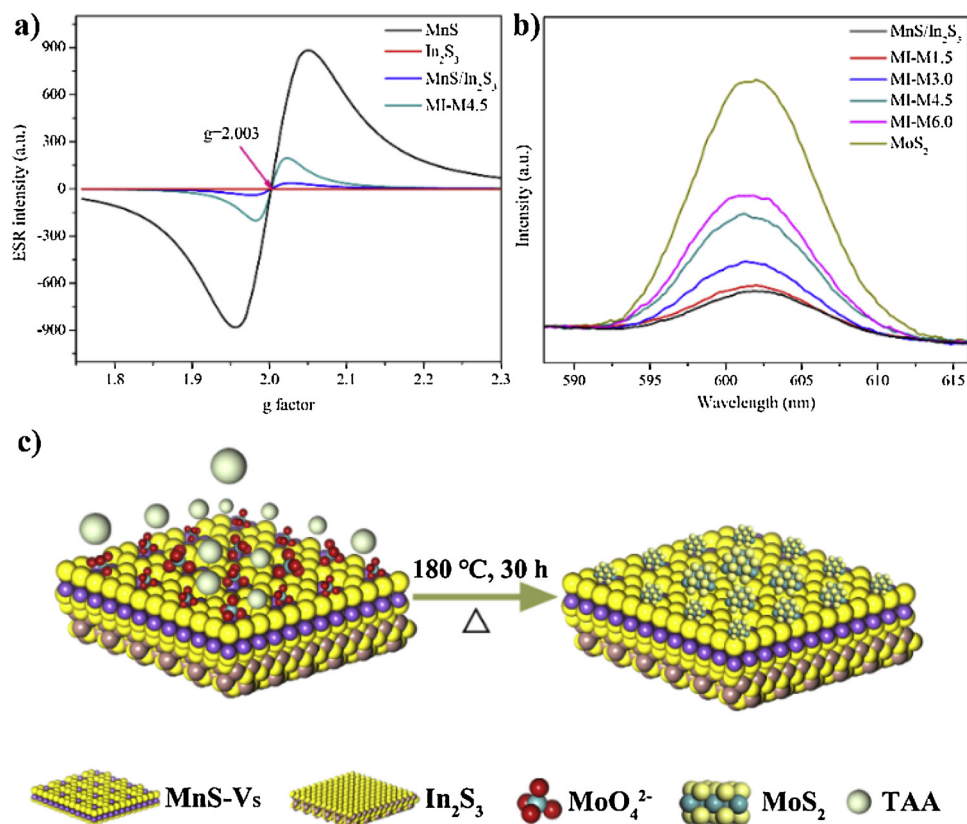
**Fig. 1.** a) Room-temperature ESR spectra; b) PL spectra of the samples, c) Formation mechanism of MI-M composites.
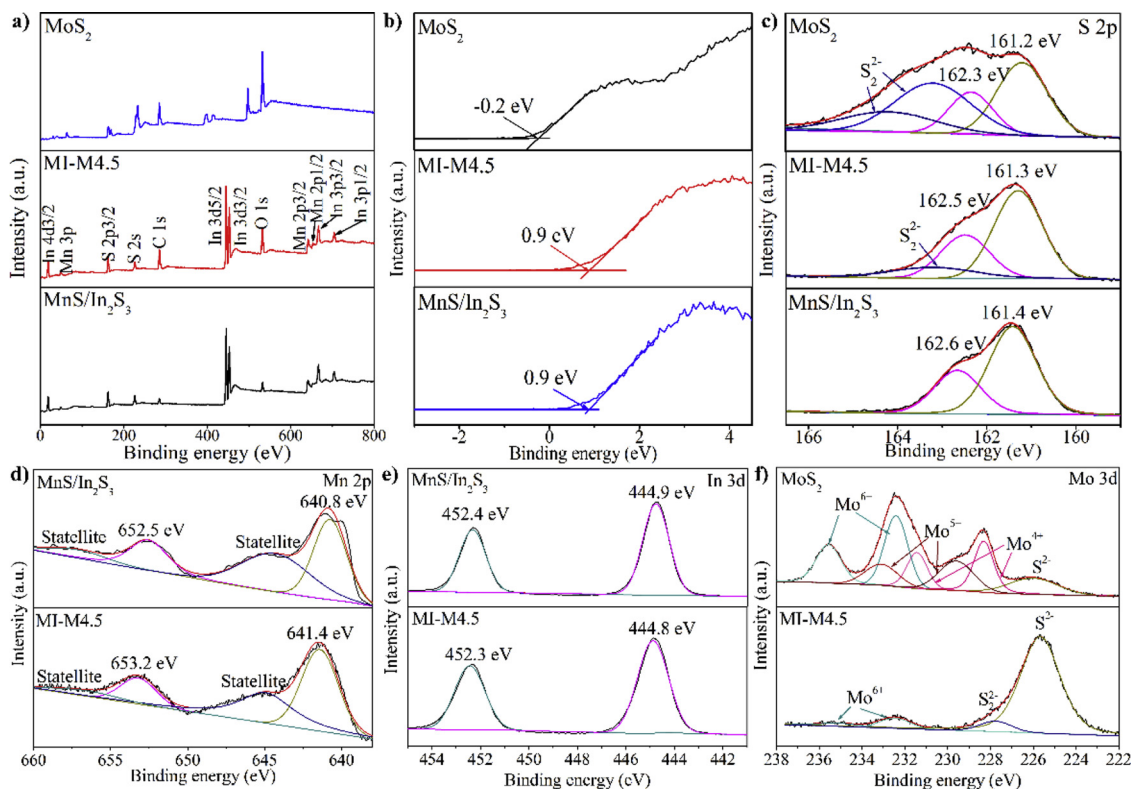


**Fig. 2.** a) XPS survey spectra; b) Valence-band XPS spectra; c) S 2p; d) Mn 2p e); In 3d; f) Mo 3d XPS spectra of the MnS/In$_2$S$_3$, MoS$_2$, and MI-M4.5.
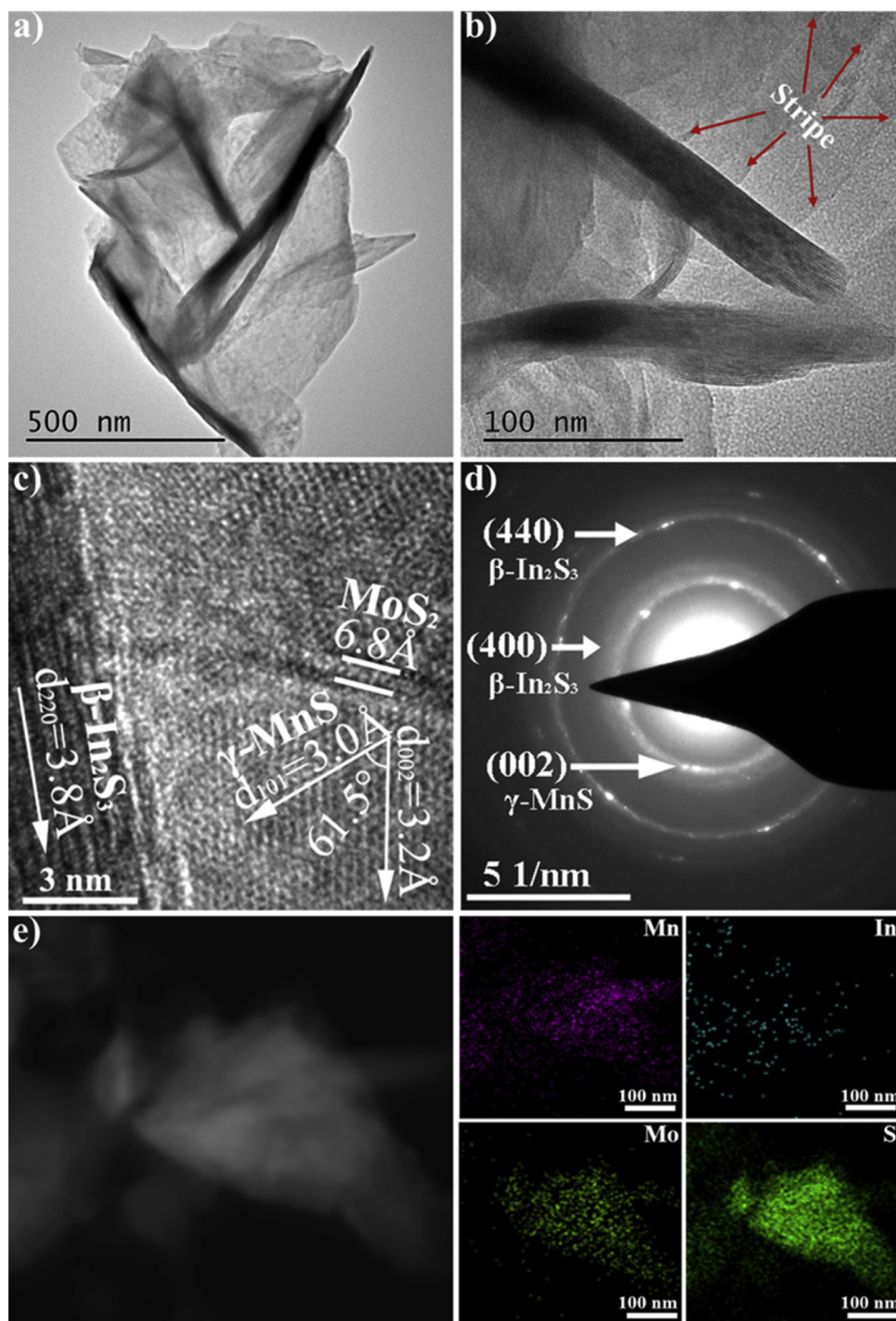
**Fig. 3.** a, b) TEM and c) HRTEM image of MI-M4.5; d) SAED patterns of MI-M4.5.

by the $N_2$ adsorption-desorption experiments (Fig. S6). It is noteworthy that some stripe and wrinkled regions can be observed on $MnS/In_2S_3$ nanosheet surface (Fig. 3b), which may be derived from the $MoS_2$. The lattice spacing corresponding to MnS and $\beta$-$In_2S_3$ can be simultaneously found in Fig. 3c. From the HRTEM image, it is recognizable that the $\gamma$-MnS is in close contact with $\beta$-$In_2S_3$ to form layered heterostructures. Specifically, the wrinkled regions with the lattice spacing identical to 6.8 Å, which is ascribed to the (002) plane of hexagonal $MoS_2$, is observed. It is noted that the single (few)-layer $MoS_2$ can be clearly found in MnS region (cf. Fig. 3c). However, the clear diffraction ring of $MoS_2$ is not found (Fig. 3d) indicates the low crystalline of $MoS_2$, which can be attributed to the formation of rich $U_S$ defects $MoS_2$ in MI-M

composites. Moreover, EDS elemental mapping images clearly show the distribution of each element in the MC-M4.5 composite, confirming the existence of Mn, In, Mo, and S, as shown in Fig. 3e. Notably, Mn and Mo exhibit the similar distribution, and In appears at different sites, which provides a direct evidence to further demonstrate the unsaturated-sulfur-edge-rich $MoS_2$ can selectively grow on the MnS of $MnS/In_2S_3$ composite. These results elaborate that the MI-M double-interface-structure with an intimate contact can be effectively constructed by selective decoration of single (few)-layer $MoS_2$ on MnS in $MnS/In_2S_3$ composite.

To shed light on the advantage of the novel MI-M composites, the photocatalytic performance of the as-prepared samples was evaluated
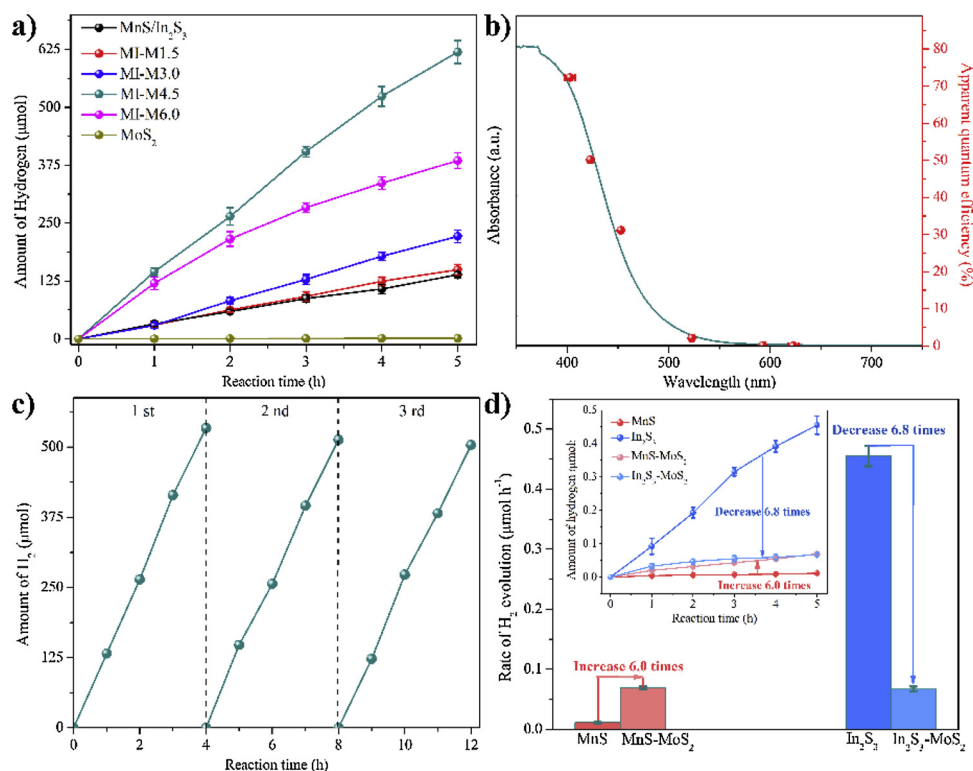
**Fig. 4.** a) Photocatalytic $H_2$ production over all tested samples under visible light irradiation ($\lambda > 420$ nm); b) Wavelength-dependent AQE of photocatalytic $H_2$ evolution over MI-M4.5 together with its UV–vis diffuse reflectance spectra (UV–vis DRS); c) Cycling tests; d) Photocatalytic $H_2$ production over MnS, MnS-$MoS_2$, $In_2S_3$ and $In_2S_3$-$MoS_2$ under visible-light irradiation ($\lambda > 420$ nm).
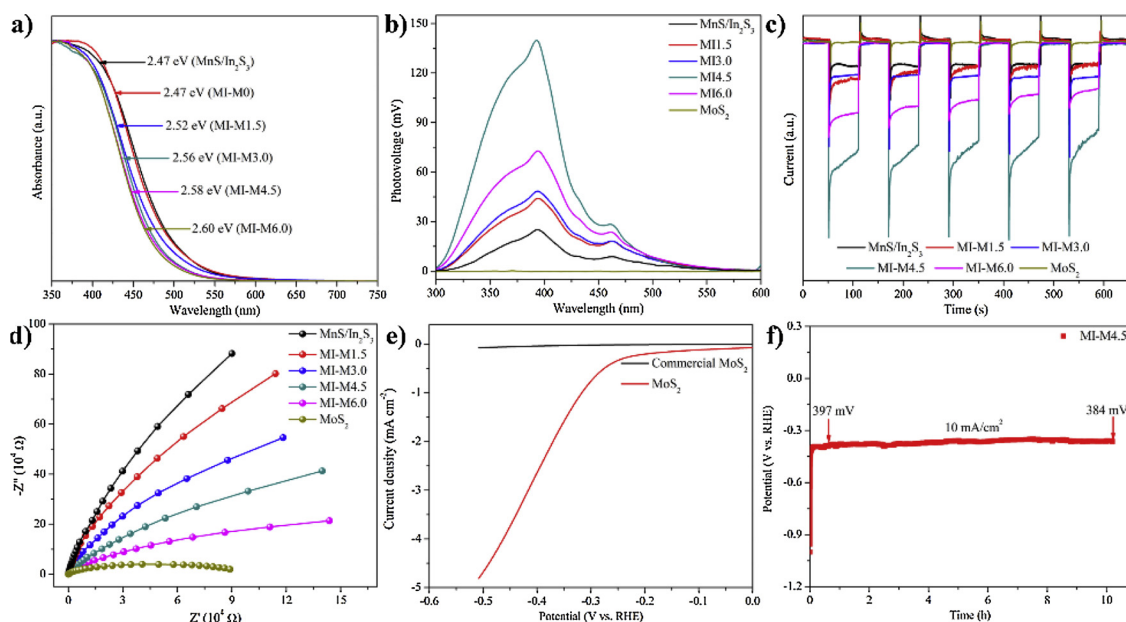


**Fig. 5.** a) UV–vis DRS; b) SPV spectrum; c) Transient photocurrent response; d) EIS of all the prepared samples; e) Linear sweep voltammetry curves of commercial $MoS_2$ and $MoS_2$; f) Chronopotentiometric curve of MI-M4.5 samples in 1.2 M $Na_2SO_3$.

by $H_2$ production from waste $H_2S$ under visible-light irradiation ($\lambda > 420$ nm) in a home-made photoreactor (50 mL Pyrex flask), as shown in Fig. S7. The blank experiments reveal that $H_2$ is not evolved in the absence of either photocatalyst or light illumination. Fig. 4a and Fig. S8 shows the PHP performance of MI-M composites with different $MoS_2$ loading amounts, which approves that the photocatalytic $H_2S$ splitting performance of MnS/$In_2S_3$ is remarkably enhanced through the introduction of $MoS_2$. Specially, the highest photocatalytic $H_2S$ splitting activity with $H_2$ production rate of 124 μmol h$^{-1}$ was achieved over MI-M4.5, which is ca. 4.5 times higher than that of the MnS/$In_2S_3$ (28 μmol h$^{-1}$). The AQY of MI-M4.5 at 400 and 420 nm are as high as

72% and 50%, respectively (Table S1). This is the highest visible-light-driven $H_2S$ splitting efficiency reported so far among all non-noble-metal photocatalysts (Table S2). Further increasing the content of $MoS_2$ in MnS/$In_2S_3$ results in the descending amount of $H_2$ production which is below 77 μmol h$^{-1}$ over MI-M6.0, owing to a "shielding effect" of $MoS_2$ for hampering the sunlight absorption [46]. The individual $MoS_2$ exhibits a trace amount of $H_2$ evolution, authenticating the role of $MoS_2$ as the cocatalyst in MI-M composite. It can be concluded from the above results that the double-interface-structure and rich catalytically active sites in architecting photocatalysts are vital for the application in superior photocatalytic $H_2S$ splitting. Meanwhile, AQE is found to track
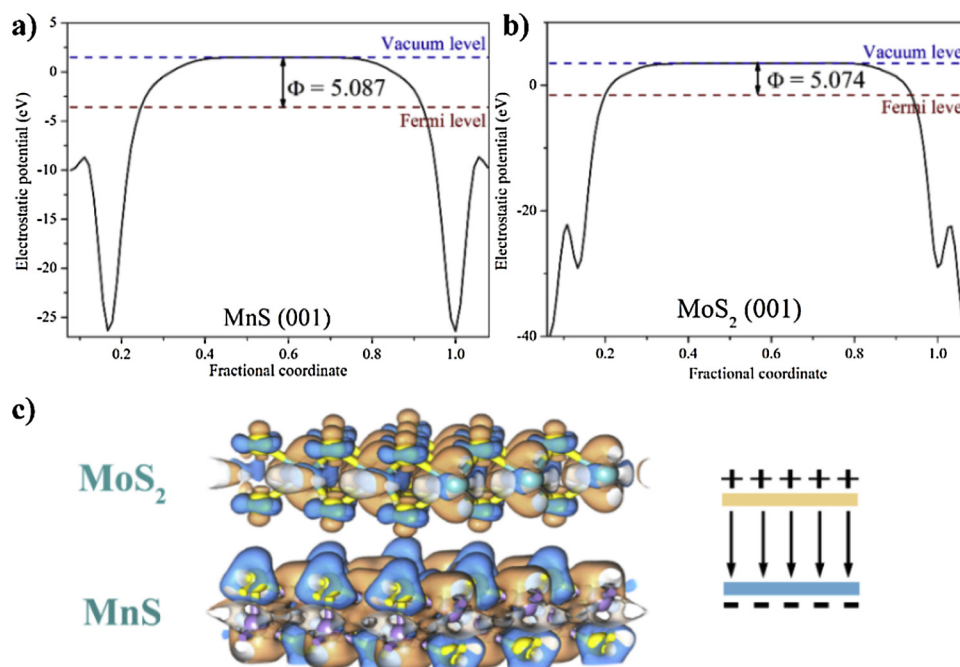
Fig. 6. Work functions of (a) MnS (001) and b) MoS$_2$ (001); (c) The charge density difference map of MnS/MoS$_2$.

the UV–vis DRS of MI-M4.5 (Fig. 4b), confirming the photocatalytic nature of the H$_2$ production over MI-M composites. Moreover, the photostability is also a crucial factor for the practical applications. There is negligible decrease in the rates of H$_2$ production in three consecutive runs of accumulatively 12 h visible-light irradiation (Fig. 4c). Furthermore, the crystal structure does not change after cycling tests (Fig. S9), suggesting the MI-M composites possess an excellent photostability during the photocatalytic H$_2$S splitting process. In addition, the comparison experiment was also performed to lend support to much easier decoration of MoS$_2$ on MnS as compared to In$_2$S$_3$ in MI-M composite. As shown in Fig. 3d, the MnS-MoS$_2$ composite exhibits enhanced photocatalytic hydrogen evolution efficiency (0.07 μmol h$^{-1}$), which is 7 orders of magnitude higher than that of the pristine MnS (0.01 μmol h$^{-1}$). However, the introduction of MoS$_2$ significantly inhibits the catalytic activity of the pristine In$_2$S$_3$ (0.46 μmol h$^{-1}$) by about 7 times. It is, therefore, again pertinent that the MoS$_2$ is more prone to anchor on MnS than In$_2$S$_3$ in MI-M composites.

The photocatalytic H$_2$S splitting in the present system involves consecutive steps such as sunlight absorption by catalysts to generate photoinduced electron-hole pairs in the bulk, separation of exited charges and migration to the surface, and surface redox reaction [26,46–48]. The sunlight-harvesting capability of the as-prepared samples can be accessed by UV–vis DRS. As revealed by Fig. 5a and Fig. S10, the absorption edges of MI-M samples become steeper with increasing the loaded amount of MoS$_2$, which may be due to that the Vs on the MnS/In$_2$S$_3$ can be filled by the Vs-selectively anchoring of MoS$_2$. In addition to the optical properties, the charge separation and transport performance were exploited through SPV spectrum, transient photocurrent response and EIS. As exhibited in Fig. 5b, all the MI-M samples show an enhanced SPV response as compared to the pristine MnS/In$_2$S$_3$. Nevertheless, the MoS$_2$ itself does not show obvious SPV response. The results confirm that the introduction of MoS$_2$ can significantly promote the charge carrier separation and migration because MoS$_2$ plays an important role to accept photo-generated electrons. Among these samples, MI-M4.5 has the highest SPV response, indicating the highly efficient separation of photo-generated electron and hole pairs. Indeed, the SPV response intensity is in line with the photocatalytic activity. A similar result is observed in the transient

photocurrent response and EIS tests (Fig. 5c-d). It is worthwhile mentioning that the single MoS$_2$ shows the smallest arc radius of the Nyquist plot, suggesting a superior electron conductivity, which is fundamentally crucial to efficiently capture the photoinduced electrons from MnS in MI-M composite to prevent the recombination of charge carriers. To further confirm the U$_S$-rich MoS$_2$ can act as suitable cocatalyst for promoting H$_2$ production performance. First, the proton reduction activity of commercial MoS$_2$ and U$_S$-rich MoS$_2$ is investigated by LSV approach [1,4,49–52]. As shown in Fig. 5e, the U$_S$-rich MoS$_2$ exhibits a very strong reduction current and a lower onset potential for H$_2$ evolution (only -0.27 V vs. RHE, calculated through the intercept of the plot tangents on horizontal axis) as compared with the commercial MoS$_2$ (-0.31 V vs. RHE), illustrating the U$_S$-rich MoS$_2$ process an excellent proton reduction ability. This point is well verified by comparing with the LSV curves of MnS/In$_2$S$_3$ and MI-M4.5 (Fig. S11), because the onset overpotential of MnS/In$_2$S$_3$ sample (-0.47 V vs. RHE) can be obviously decreased by the introduction of U$_S$-rich MoS$_2$ to form the novel MI-M4.5 (-0.41 V vs. RHE) (Fig. S11), confirming the proton reduction ability of MnS/In$_2$S$_3$ composite can be significantly improved by the introduction of U$_S$-rich MoS$_2$. It is noteworthy that the onset overpotential of MnS/In$_2$S$_3$ and MI-M4.5 can be further decreased under visible-light irradiation (Fig. S11), the corresponding onset overpotential of MI-M4.5 at 0.24 V vs. RHE was improved about 41%, which is much larger than that of MnS/In$_2$S$_3$ composite (28%), indicating the photocatalytic H$_2$ evolution ability of MnS/In$_2$S$_3$ composite can be efficiently improved by the introduction of U$_S$-rich MoS$_2$, which accordance with the result of photocatalytic H$_2$ production activity. Moreover, the long-term stability of MI-M4.5 photocatalysts is further determined by using chronopotentiometry method at the current density of 10 mA cm$^{-2}$ for 10 h, as shown in Fig. 5f. During the test, the overpotential for H$_2$ production on MI-M4.5/ITO electrode only slightly decreased from the initial ca. 397 to ca. 384 mV (Fig. 5f), indicating the excellent stability of the MI-M4.5 catalyst under the reaction process.

The DFT calculation was performed to further investigate the photoinduced electron process. Generally, the charge transfer process is work function (Φ) dependent when the two semiconductors come in contact [53,54]. This denotes that the electrons would transfer from low Φ catalysts to high Φ catalysts until their Femi level are aligned at the same level, resulting in a built-in electric field at the interface
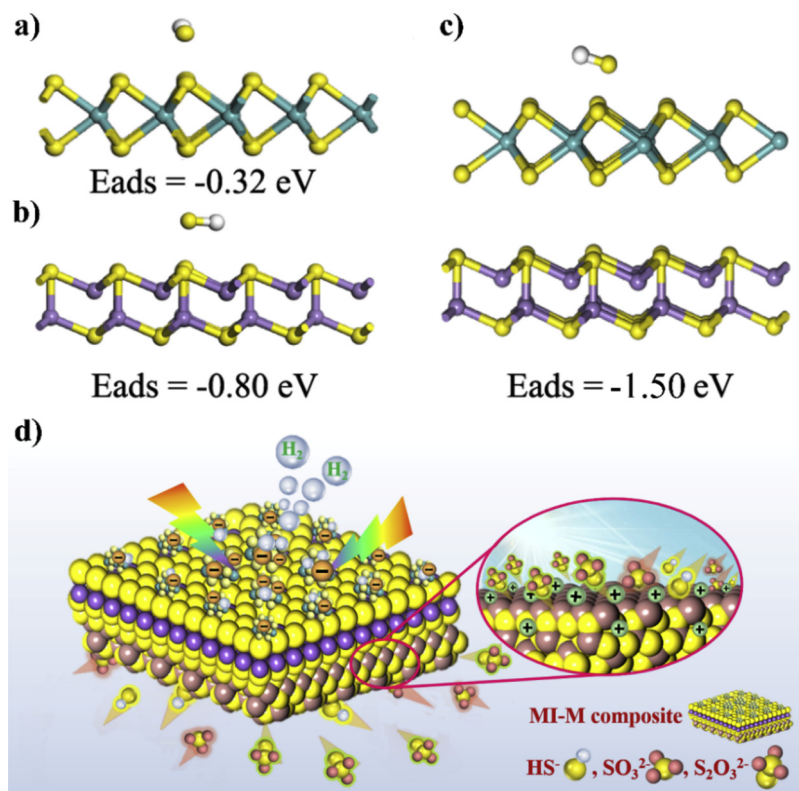
**Fig. 7.** The structures of HS$^-$ adsorbed on the surface of (a) MoS$_2$ (001), (b) MnS (001) and (c) MnS-MoS$_2$; d) Schematic illustration of the PHP mechanism in MI-M composite.

[53,54]. As displayed in Fig. 6a-b, the work function of MnS (001) and MoS$_2$ (001) estimated by the DFT calculations is 5.087 and 5.074 eV, respectively. Upon the contact of MnS and MoS$_2$, the electrons tend to migrate from MoS$_2$ to MnS to achieve Fermi level equilibrium between them. Accordingly, the interface of MnS/MoS$_2$ is charged, stimulating the formation of an internal electric field pointing from MoS$_2$ to MnS, accelerating the charge carrier migration between MnS and MoS$_2$. This result is further validated by the charge density difference map of MnS/MoS$_2$ ((Fig. 6c). The existence of internal electric field directing from MoS$_2$ to MnS in the present system is especially significant. When MI-M samples were irradiated by a photon with sufficient energy equal or larger than Eg, both MnS and In$_2$S$_3$ are excited to generate electrons and holes which are directionally separated by the internal electric field between MnS and In$_2$S$_3$. The electrons being separated can further migrate to MoS$_2$ nanosheet due to the existence of internal electric field pointing from MoS$_2$ to MnS. Therefore, the formation of MI-M double-interface-structure is inspiring which enables lengthen the recombination distance of electron-hole pairs significantly and thereby leads to the superior separation ability of photogenerated charges.

Given that the adsorption of HS$^-$ is the first important step for photocatalytic reaction, the effect of MoS$_2$ loading on surface reaction is investigated with HS$^-$ adsorption performance on the basis of DFT calculations, as shown in Fig. 7a-c. The HS- adsorption performance is evaluated by the adsorption energy ($E_{ads}$) calculated using the Eq. (2):

$$E_{ads} = E_{slab+adsorbate} - E_{adsorbate} - E_{slab} \qquad (2)$$

Where $E_{slab+adsorbate}$ and $E_{slab}$ are the total energies of the substrate with and without the adsorbates respectively, and $E_{adsorbate}$ is the energy of adsorbed species. The $E_{ads}$ of HS$^-$ adsorbed on the surface of MoS$_2$ (001), MnS (001) and MnS-MoS$_2$ are -0.32, -0.80 and -1.50 eV, respectively. These results clearly confirmed that the HS$^-$ adsorption is much easier occurring on the surface of MnS-MoS$_2$ than MnS and MoS$_2$. Hence, the introduction of MoS$_2$ could promote HS$^-$ adsorption. Finally, the photogenerated electrons on the unsaturated-sulfur-edge of

MoS$_2$ are involved in the superior photocatalytic H$_2$ evolution from waste H$_2$S splitting (2H$^+$ + 2e$^-$ → H$_2$). The photogenerated holes on In$_2$S$_3$ are consumed by the oxidization reaction (HS- + 2 h$_{VB}^+$ → H$^+$ + S, SO$_3^{2-}$ + S$^{2-}$ + 2 h$_{VB}^+$ → S$_2$O$_3^{2-}$) [36], thus further improving the separation of electron and hole pairs (Fig. 7d).

## 4. Conclusion

In summary, novel MI-M composites have been smartly constructed by a facile defect-induced growth strategy. Both experimental and theoretical calculation results proved that the Vs in MnS of MnS/In$_2$S$_3$ can serve as anchoring sites to realize selectively decorating of the U$_S$-rich MoS$_2$ on MnS in MnS/In$_2$S$_3$, and thus forming a double-interface-structure. Hence, the cocatalysts effect of MoS$_2$ can be vastly developed, which achieves three prominent advantages in improving the photocatalytic H$_2$S splitting performance: (i) facilitating charge separation and migration, (ii) providing rich catalytically active sites, and (iii) enhancing HS$^-$ adsorption on the catalyst surface. As a result, the MI-M composite showed a state-of-the-art photocatalytic H$_2$ evolution activity (124 μmol h$^{-1}$) from waste H$_2$S, which is almost 4.5 times higher than that of the MnS/In$_2$S$_3$ composite. The corresponding AQE at 400 nm is 72.3%, which is the highest visible-light-driven photocatalytic H$_2$S splitting efficiency reported so far among all kinds of non-noble-metal photocatalysts. In addition, the superior performance of MI-M composites is also demonstrated by the electrochemical H$_2$ evolution tests. The significance of this research aims to provide an elegant strategy for anchoring transition metal dichalcogenide cocatalysts with rich reaction active sites on metal sulfide composites to form the double-interface-structure for robust resource utilization of H$_2$S and other photocatalytic reactions.

## Conflict of interest

The authors declare no conflict of interest.

## Acknowledgements

## Appendix A. Supplementary data

Supplementary material related to this article can be found, in the online version, at doi:https://doi.org/10.1016/j.apcatb.2019.117870.

## References

[1] X. Zhang, Y.Y. Tang, S.Q. Qu, J.W. Da, Z.P. Hao, ACS Catal. 5 (2015) 1053–1067.
[2] A.P. Reverberi, J.J. Klemeš, P.S. Varbanov, B. Fabiano, J. Clean. Prod. 136 (2016) 72–80.
[3] J.J. Zhang, H. Wang, X.Z. Yuan, G.G. Zeng, W.G. Tu, S.B. Wang, J. Photoch. Photobio. C 38 (2019) 1–26.
[4] X. Zong, J.F. Han, B. Seger, H.J. Chen, G.Q. Lu, C. Li, L. Wang, Angew. Chem. Int. Ed. 53 (2014) 4399–4403.
[5] A. Prakash, M. Dan, S. Yu, S.Q. Wei, Y. Li, F. Wang, Y. Zhou, Sol. Energ. Mat. Sol. C. 180 (2018) 205–212.
[6] Y. Li, S. Yu, D.E. Doronkin, S.Q. Wei, M. Dan, F. Wu, L.Q. Ye, J.-D. Grunwaldt, Y. Zhou. J. Catal. 373 (2019) 48–57.
[7] G. Ma, H. Yan, J. Shi, X. Zong, Z. Lei, C. Li, J. Catal. 260 (2008) 134–140.
[8] M. Dan, S.Q. Wei, D.E. Doronkin, Y. Li, Z.Y. Zhao, S. Yu, J.-D. Grunwald, Y.H. Lin, Y. Zhou. Appl. Catal. B: Environ. 243 (2019) 790–800.
[9] L. Cheng, Q.J. Xiang, Y. Liao, H.W. Zhang, Energy Environ. Sci. 11 (2018) 1362–1391.
[10] H. He, J. Cao, M. Guo, H. Lin, J. Zhang, Y. Chen, S. Chen, Appl. Catal. B: Environ. 249 (2019) 246–256.
[11] M. Dan, A. Prakash, Q. Cai, J.L. Xiang, Y.H. Ye, Y. Li, S. Yu, Y.H. Lin, Y. Zhou, Sol. RRL 3 (2019) 1800237.
[12] B. Wang, S. He, L.L. Zhang, X.Y. Huang, F. Gao, W.H. Feng, P. Liu, Appl. Catal. B: Environ. 243 (2019) 229–235.
[13] S. Ida, K. Sato, T. Nagata, H. Hagiwara, M. Watanabe, N. Kim, Y. Shiota, M. Koinuma, S. Takenaka, T. Sakai, E. Ertekin, T. Ishihara, Angew. Chem. Int. Ed. 57 (2018) 1–6.
[14] X. She, H. Xu, L. Li, Z. Mo, X. Zhu, Y. Yu, Y. Song, J. Wu, J. Qian, S. Yuan, H. Li, Appl. Catal. B: Environ. 245 (2019) 477–485.
[15] X.C. Wang, K. Maeda, X.F. Chen, K. Takanabe, K. Domen, Y.D. Hou, X.Z. Fu, M. Antonietti, J. Am. Chem. Soc. 131 (2009) 1680–1681.
[16] B.J. Ng, L.K. Putri, X.Y. Kong, K.P.Y. Shak, P. Pasbakhsh, S.P. Chai, A.R. Mohamed, Appl. Catal. B: Environ. 224 (2018) 360–367.
[17] D.J. Martin, P.J.T. Reardon, S.J.A. Moniz, J. Tang, J. Am. Chem. Soc. 136 (2014) 12568–12571.
[18] D.V. Esposito, S.T. Hunt, A.L. Stottlemyer, K.D. Dobson, B.E. McCandless, R.W. Birkmire, J.G.G. Chen, Angew. Chem. Int. Ed. 49 (2010) 9859–9862.
[19] Y. Jiao, Y. Zheng, M. Jaroniec, S.Z. Qiao, Chem. Soc. Rev. 44 (2015) 2060–2086.
[20] Q. Li, L.H. Wu, G. Wu, D. Su, H.F. Lv, S. Zhang, W.L. Zhu, A. Casimir, H.Y. Zhu, A. Mendoza-Garcia, S.H. Sun, Nano Lett. 15 (2015) 2468–2474.
[21] Y. Shi, Y. Zhou, D.R. Yang, W.X. Xu, C. Wang, F.B. Wang, J.J. Xu, X.H. Xia, H.Y. Chen, J. Am. Chem. Soc. 139 (2017) 15479–15485.
[22] H. Li, C. Tsai, A.L. Koh, L.L. Cai, A.W. Contryman, A.H. Fragapane, J.H. Zhao, H.S. Han, H.C. Manoharan, F. Abild-Pedersen, J.K. Nørskov, X.L. Zheng, Nat. Mater. 15 (2016) 48–53.
[23] B. Hinnemann, P.G. Moses, J. Bonde, K.P. Jørgensen, J.H. Nielsen, S. Horch, I. Chorkendorff, J.K. Nørskov, J. Am. Chem. Soc. 127 (2005) 5308–5309.
[24] S.Z. Yang, Y.J. Gong, P. Manchanda, Y.Y. Zhang, G.L. Ye, S.M. Chen, L. Song, S.T. Pantelides, P.M. Ajayan, M.F. Chisholm, W. Zhou, Adv. Mater. 30 (2018) 1803477.
[25] T.F. Jaramillo, K.P. Jørgensen, J. Bonde, J.H. Nielsen, S. Horch, I. Chorkendorff, Science 317 (2007) 100–102.
[26] D.P. Kumar, S. Hong, D.A. Reddy, T.K. Kim, Appl. Catal. B: Environ. 212 (2017) 7–14.
[27] X. Zong, H.J. Yan, G.P. Wu, G.J. Ma, F.Y. Wen, L. Wang, C. Li, J. Am. Chem. Soc. 130 (2008) 7176–7177.
[28] K. Chang, X. Hai, H. Pang, H.B. Zhang, L. Shi, G.G. Liu, H.M. Liu, G.X. Zhao, M. Li, J.H. Ye, Adv. Mater. 28 (2016) 10033–10041.
[29] U. Maitra, U. Gupta, M. De, R. Datta, A. Govindaraj, C.N.R. Rao, Angew. Chem. Int. Ed. 125 (2013) 13295–13299.
[30] Y.J. Yuan, P. Wang, Z.J. Li, Y.Z. Wu, W.F. Bai, Y.B. Su, J. Guan, S.T. Wu, J.S. Zhong, Z.T. Yu, Z.G. Zou, Appl. Catal. B: Environ. 242 (2019) 1–8.
[31] Y.J. Yuan, Y. Yang, Z.J. Li, D.Q. Chen, S.T. Wu, G.L. Fang, W.F. Bai, M.Y. Ding, L.X. Yang, D.P. Cao, Z.T. Yu, Z.G. Zou, ACS Appl. Energy Mater. 1 (2018) 1400–1407.
[32] K. Zhang, J.K. Kim, B. Park, S. Qian, B.J. Jin, X.W. Sheng, H.B. Zeng, H.J. Shin, S.H. Oh, C.L. Lee, J.H. Park, Nano Lett. 17 (2017) 6676–6683.
[33] S.Q. Zhang, X. Liu, C.B. Liu, S.L. Luo, L.L. Wang, T. Cai, Y.X. Zeng, J.L. Yuan, W.Y. Dong, Y. Pei, Y.T. Liu, ACS Nano 12 (2018) 751–758.
[34] Y.J. Yuan, Z.J. Li, S.T. Wu, D.Q. Chen, L.X. Yang, D.P. Cao, W.G. Tu, Z.T. Yu, Z.G. Zou, Chem. Eng. J. 350 (2018) 335–343.
[35] Y.J. Yuan, Z.K. Shen, S.T. Wu, Y.B. Su, L. Pei, Z.G. Ji, M.Y. Ding, W.F. Bai, Y.F. Chen, Z.T. Yu, Z.G. Zou, Appl. Catal. B: Environ. 246 (2019) 120–128.
[36] M. Dan, Q. Zhang, S. Yu, A. Prakash, Y.H. Lin, Y. Zhou, Appl. Catal. B: Environ. 217 (2017) 530–539.
[37] J.P. Perdew, K. Burke, M. Ernzerhof, Phys. Rev. Lett. 77 (1996) 3865–3868.
[38] M.D. Segall, P.J.D. Lindan, M.J. Probert, C.J. Pickard, P.J. Hasnip, S.J. Clark, M.C. Payne, J. Phys-Condens. Mat. 14 (2002) 2717–2744.
[39] Y.F. Huang, R.J. Nielsen, W.A. Goddard III, J. Am. Chem. Soc. 140 (2018) 16773–16782.
[40] D.W. Hall, N.F. Borrelli, J. Opt. Soc. Am. B 5 (1988) 1650–1654.
[41] Z.B. Fang, X.Y. Huang, Y.Z. Wang, W.H. Feng, Y. Zhang, S.X. Weng, X.Z. Fu, P. Liu, J. Mater. Chem. A 4 (2016) 13980–13988.
[42] X.L. Fu, L. Zhang, L.H. Liu, H. Li, S.G. Meng, X.J. Ye, S.F. Chen, J. Mater. Chem. A 5 (2017) 15287–15293.
[43] M.L. Tang, D.C. Grauer, B. Lassalle-Kaiser, V.K. Yachandra, L. Amirav, J.R. Long, J. Yano, A.P. Alivisatos, Angew. Chem. Int. Ed. 123 (2011) 10385–10389.
[44] L.R.L. Ting, Y.L. Deng, L. Ma, Y.J. Zhang, A.A. Peterson, B.S. Yeo, ACS Catal. 6 (2016) 861–867.
[45] P.D. Tran, T.V. Tran, M. Orio, S. Torelli, Q.D. Truong, K. Nayuki, Y. Sasaki, S.Y. Chiam, R. Yi, I. Honma, J. Barber, V. Artero, Nat. Mater. 15 (2016) 640–646.
[46] J.X. Low, J.G. Yu, M. Jaroniec, S. Wageh, A.A. Al-Ghamdi, Adv. Mater. 29 (2017) 1601694.
[47] P. Ganguly, C. Byrne, A. Breen, S.C. Pillai, Appl. Catal. B: Environ. 225 (2018) 51–75.
[48] N.C. Zheng, T. Ouyang, Y. Chen, Z. Wang, D. Chen, Z.Q. Liu, Catal. Sci. Technol. 9 (2019) 1357–1364.
[49] Z. Chen, T.F. Jaramillo, T.G. Deutsch, A. Kleiman-Shwarsctein, A.J. Forman, N. Gaillard, R. Garland, K. Takanabe, C. Heske, M. Sunkara, J. Mater. Res. 2 (2010) 3–16.
[50] F.E. Osterloh, ACS Energy Lett. 2 (2017) 445–453.
[51] K. Takanabe, J. Catal. 370 (2019) 480–484.
[52] J.G. Wang, Y.J. Chen, W. Zhou, G.H. Tian, Y.T. Xiao, H.Y. Fu, H.G. Fu, J. Mater. Chem. A 5 (2017) 8451–8460.
[53] J.X. Low, B.Z. Dai, T. Tong, C.J. Jiang, J.G. Yu, Adv. Mater. 31 (2018) 1802981.
[54] Q.L. Xu, B.C. Zhu, C.J. Jiang, B. Cheng, J.G. Yu, Sol. RRL 2 (2018) 1800006.